Composite Control Arm Design: A Comprehensive Workflow

2021-21M-0045

Composite Control Arm Design: A Comprehensive Workflow

Author, co-author (Do NOT enter this information. It will be pulled from participant tab in MyTechZone)
Affiliation (Do NOT enter this information. It will be pulled from participant tab in MyTechZone)

Abstract

This paper presents a complete overview of the computational design of an advanced suspension control arm constructed of composite material for light weighting purposes. The proposed methodology, presented in detail, is split into 4 stages: Pre-Engineering, in which basic modelling and a sensibility study is performed to better understand the advantages of unsprung mass reduction (compared to sprung mass reduction) with respect to the vehicle's vertical dynamics, as well as to set objectives for the study. Engineering Phase 1, representing the development and utilization of a multibody approach to evaluate the full-vehicle response to different dynamic maneuvers, such as harsh road imperfections, sine sweep steering, and double lane change tests. The impact of the improved suspension control arm is highlighted in detail, and the loads to which it is subjected are computed to serve as inputs for the successive phases. Engineering Phase 2, where a closer look is given to the structural side of the component, understanding the specific behavior of composite materials and performing modelling of the control arm, followed by fine tuning with Finite Element Method optimization techniques. This phase consists of a topology optimization, followed by composite topography free size, size, and shuffle optimizations to arrive upon the ideal part-layup, and guarantee the desired mechanical characteristics of the component. Lastly, the Final Engineering Phase closes the design process by generating the production processes, steps, constraints and tooling for the correct realization of the innovative control arm in a real-world application. The tools presented in this paper were created to allow the design to be completed rapidly, thus defining a blueprint for a full workflow, from engineering request to product delivery, which can be applied to different vehicles and customer requests, representing an essential step forward to the consolidation of the use of composite materials for structural suspension components.

Introduction

Vehicle mass reduction is becoming increasingly important due to current regulations and climate increasingly pushing the importance on fuel efficiency, and reduction of vehicle consumables such as brakes and tires [1,2]. Mass reduction offers a unique opportunity to increase both efficiency and performance simultaneously. Lighter vehicle weights can be achieved by optimizing design, using higher performance construction methods, or changing product goals and requirements. To avoid the latter, OEMs are dedicating increasing amounts of resources towards the first two options.

When individual components of a vehicle come under light weighting scrutiny, the large, heavy, easy, parts understandably tend to be addressed first [3–5], while only the more complex, dangerous, difficult parts are passed over, especially in the absence of advanced monitoring techniques [6]. As more areas of the vehicle are being lightened, previously overlooked parts, such as suspension members, become more appealing targets.

Of particular interest is the suspension system [7,8], which has seen less significant lightening, compared with other areas, in most production vehicles over the last decades. Composite materials' usefulness in light weighting has been of attention to the automotive world since the 1941 Ford "Soybean Car" first introduced

them [9], yet the suspension area has been relatively void of notable applications, apart from Corvette's use of glass fiber reinforced polymer leaf springs and evolutions of leaf spring concepts [10].

In order to explore the application of composites to suspension members, a hypothetical front upper control arm for a second-generation Audi R8 V10 is designed. The study presented is divided into three parts, the first of which is a benefit analysis. A highly simplified suspension model is created using MATLAB programming, and an Adams Car multibody model is created to investigate further than the well-known benefits of simple mass reduction; specifically, the relative benefit of unsprung versus sprung mass reduction are analyzed. Next, a finite element analysis composite optimization process is utilized to help design the part as light as possible using modern construction techniques. Lastly, production tooling is created to demonstrate how a similar approach to design could be taken by a client to get to market in a straightforward, guided, and cost-efficient manner.

Phase 1: Vehicle Performance Simulation

Benefit Quantification

The main purpose of Phase 1 is to attempt to quantify the expected benefit of the adoption of the proposed design. The main objective of the proposed design change is a mass reduction of the control arms. This has the twin benefit of reducing both the total mass as well as the unsprung mass. The advantages of a reduction in total vehicle mass are well known, and well documented.

The amount of mass reduction possible from the conversion to composite control arms, when viewed as purely sprung mass, is not significant enough to impart a sufficiently meaningful impact on vehicle performance to make financial sense. The advantages of the possible reduction in unsprung mass, however, are more significant [11]. An emphasis on the reduction of unsprung mass is common practice, however, there is very little published, concrete, documentation as to the objective benefits of this type of mass reduction. A study conducted by Lotus Cars touched on their extensive use of expert test drivers to gauge the effect of the addition of 20kg per corner of unsprung mass, yet this is subjective feedback [12]. Often the focus in this area is specifically with respect to the wheels, which are not only unsprung, but also rotational, mass. Rotational mass brings along a plethora of other detriments, due not only to the rotational inertia's effect on the acceleration and deceleration of rotating bodies, but also the increase in gyroscopic effect. These further obscures the understanding of the true importance of unsprung mass. Thus, a more general objective of this phase is to investigate exactly how much unsprung mass reduction improves handling and comfort.

First, a quantization method is developed to objectively determine improvements in handling and comfort. The comfort measurements the process is relatively straightforward. The discomfort experienced by a vehicle's occupant is related directly to the forces exerted on their body. These forces are derived from the body accelerations. The suspension is correlated to these accelerations primarily in the vertical direction; thus, the vertical acceleration of the sprung mass is taken as the comfort metric. This is nominated occupant discomfort for the remainder of the paper.

Differently from direct yaw control techniques [13–15], where a direct improvement on lateral dynamics is achieved, in this paper handling is measured using the concept tire load variation. One of the principal characteristics of a tire is its relationship between vertical load, F_z, and the maximum lateral force exerted, F_y. The lateral force grows linearly with vertical force, until a saturation point, when the tire can no longer support this linear relationship [16]. A metric of chassis handling competence is be the vehicle's ability to consistently work each of its tires, reaching peak load without passing into the saturation zone in F_z. Multiple factors affect this ability, such as vehicle mass, mass transfer, roll stiffness and spring stiffness, damping force, etc. Seeing as unsprung mass only has a separate effect in transient conditions (in static conditions both masses can be modeled as a singular lump), the most telling measure of its handling effect can be defined as the "bandwidth", in F_z, which is exerted on the tire over various asphalt perturbations (Figure 1). In other terms, the handling can

be quantified as the tire load variation, which is the variation in F_z due to road disturbances. This is nominated road holding disturbance for the remainder of the paper.

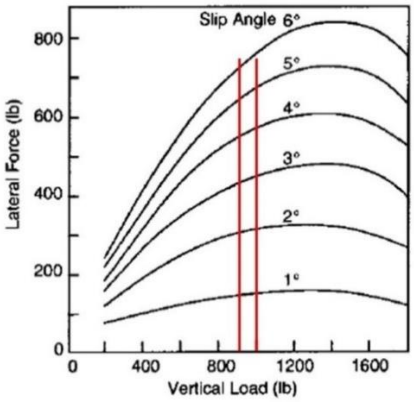

Figure 1. Tire load diagram with vertical load bandwidth due to road irregularity projected (red) adapted from [16]

Quarter Car Model

A quarter car model is adopted for the initial stages of this study. This model represents one fourth of a full car, that is, one tire, wheel, and suspension assembly, and a mass representing the relevant quarter of the vehicle body. This model is selected due to its clarity and ease of analysis, as it negates pitching and other, more complex, motions. The ability to isolate a single wheel/suspension assembly in a simple vertical motion is imperative to reducing the complexity of the post processing, and thus clearly demonstrating the behavior of the suspension, and any modification to the suspension.

Often, the quarter car is modeled as a one degree of freedom model, with a single mass, representing the vehicle body, and a single spring and damper set, representing the suspension. Due to the focus of this study (the effect of reduction of unsprung mass), a two degree of freedom model is used. This two-degree model has a mass, representing the vehicle body, a spring and damper set, representing the suspension, a second mass, representing the unsprung mass, and a second spring and damper set, representing the tire.

This model can be represented as a state space. The representation is shown in Equation (1). Z represents vertical position, k is the stiffness, m the mass, and c represents damping. Subscript “0” is the input (road profile), subscript “us” represents “unsprung mass” (that of the tire), and subscript “s” is the spring mass (that of the body).

$$\frac{d}{dt}\begin{bmatrix} z_{us}-z_0 \\ \dot{z}_{us} \\ z_s-z_{us} \\ \dot{z}_s \end{bmatrix} = \begin{bmatrix} 0 & 1 & 0 & 0 \\ -\frac{k_{us}}{m_{us}} & -\frac{c_s+c_{us}}{m_{us}} & \frac{k_s}{m_{us}} & \frac{c_s}{m_{us}} \\ 0 & -1 & 0 & 1 \\ 0 & \frac{c_s}{m_s} & -\frac{k_s}{m_s} & -\frac{c_s}{m_s} \end{bmatrix}\begin{bmatrix} z_{us}-z_0 \\ \dot{z}_{us} \\ z_s-z_{us} \\ \dot{z}_s \end{bmatrix} + \begin{bmatrix} -1 \\ \frac{c_{us}}{m_{us}} \\ 0 \\ 0 \end{bmatrix}\dot{z}_0 \quad (1)$$

The model represents only vertical movement, with no consideration for lateral or longitudinal freedom. However, for sprung mass acceleration and tire load variation, this model can be used to evaluate vehicle dynamics characteristics and can simplify such evaluation due to the lack of extraneous movements.

Handling, from the perspective of this model, concerns only the effect of road anomalies or suspension movements. This is acceptable considering the effect of unsprung mass is only significant in transient suspension conditions. By analyzing the tire squish exhibited by the model, the tire load variation can be determined. This maximum lateral force can be compromised by either too much tire load, thus tire saturation, or the lack of tire load, thus a loss of available lateral grip or complete loss of contact with the road surface.

Considering this relationship, the objective is to determine the tire load exhibited due to various “inputs”, representing the road profile. The system is subjected to a road disturbance of varying frequency and the amplitude of the sinusoidal tire variation signal is measured for with respect to the input frequency developing a frequency response. This relationship represents the relative variation in the tire deformation due to inputs (road disturbances) of different frequencies. This tire deformation is then converted into a vertical load variation via the tire stiffness. The output is a bandwidth of the tire vertical force when exposed to various frequency excitations and is used as a measure of both overall handling limit, as well as handling consistency. From here on in this phase of study, the term handling will be focused purely on the vehicle’s ability to confront transient conditions from this tire load variation perspective, without importance given to the effects of inertia in the y-axis.

During the same input sweep, the sprung mass acceleration is measured. Relating sprung mass acceleration to the frequency of road disturbance, the sprung mass acceleration transfer function is calculated and is used to determine relative comfort.

The state space of Equation (1) is converted into a MATLAB code. This code establishes the state space variables, incorporates them into a state space system, and then calculates the transfer function of the system for various frequencies. This procedure is repeated three times, each for different suspension configurations (Table 1). It is run first for a baseline system; the inputs of this system for suspension stiffness, suspension damping rate, tire stiffness, tire damping rate, unsprung mass, and sprung mass are determined by the specifications of the chosen vehicle (Audi R8 second generation), and through reasonable assumptions for unavailable data. Next, it is run for a system with a lightened unsprung mass; a mass reduction of 5 kg, representing a hypothetical exaggerated best-case scenario for the transition to all carbon control arms, was chosen. Third, it is run for a system with the unsprung mass lightened, and the sprung mass raised by the same amount. This variation (Control: Total Mass) acts as a control, allowing the decoupling of effects due to the lighter total system mass and effects due to lighter unsprung masses. Lastly, it is run for a system with the baseline unsprung mass, yet the sprung mass raised by the same 5 kg that the unsprung mass was lightened in the prior cases. This last variation (Control: Sprung Mass) acts as a second control, allowing the decoupling of effects due to heavier sprung mass and effects due to lighter unsprung masses.

Table 1. Test cases

Case	Unsprung Mass	Sprung Mass
Baseline	0	0
Lightened	-5	0
Total Mass	-5	+5
Sprung Mass	0	+5

The frequency range of interest is between 0 and 50 Hz. Below 1 Hz the movements are too slow to have a significant impact on comfort. They can have an impact on handling; however, the effects are closer to non-transient considerations thus will not be meaningfully affected by the studied modifications. Above 50 Hz is too

high to have any appreciable impact on comfort or handling due to the nature of the road excitation power spectral density [17].

The same quarter car model is created in Simulink to allow for modularity, clarity, and ease of use in future projects. The block model Simulink translation of this system is shown below (Figure 2).

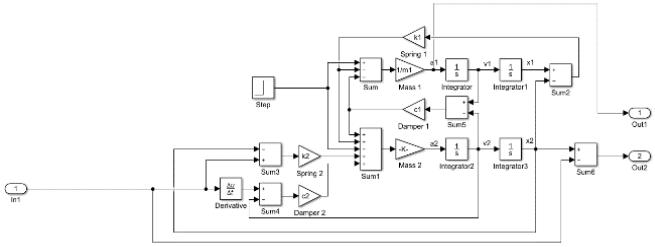

Figure 2. Simulink block representation of the quarter car model

This model simulates the 2 degree of freedom quarter car model over a road surface input. The input is a 5 mm sine wave, which gradually increases from 0 Hz to 50 Hz. Two output blocks measure the sprung mass acceleration and tire squish. Like the previous model, a baseline, a lightened, and two control systems are each included in a single simulation. This simulation is run over 5000 seconds with a timestep of 0.001 seconds. To avoid a lack of control over the model, and enable its use in generated code, a fixed time step is applied, rather than the black box “auto” option. Due to the continuous states and physical components of the model, the ODE 14x fixed-step continuous implicit solver is used. This is more stable than explicit solvers, albeit at the detriment of required computing power. The end effect is an analog of the previous model, however with a few major changes to the workflow outlined as follows. The faster, explicit and auto time step solvers are later applied and found to have similar behavior, suggesting they may be used in the future, for all but final verifications. This approach is less accurate than a state space representation. This is because it is a discretized model with the eventual, and inevitable, integration errors that accompany a model of this type. This error, however, is mitigated by using advanced integration methods, and results in little appreciable discrepancy.

The results of these simulations demonstrate variation in the metrics discussed under Benefit Quantification. For road holding disturbance there are 4 major behavior regimes: below approximately 1.7 Hz, between approximately 1.7 and 3 Hz, between approximately 3 and 15.5 Hz, and above approximately 15.5 Hz.

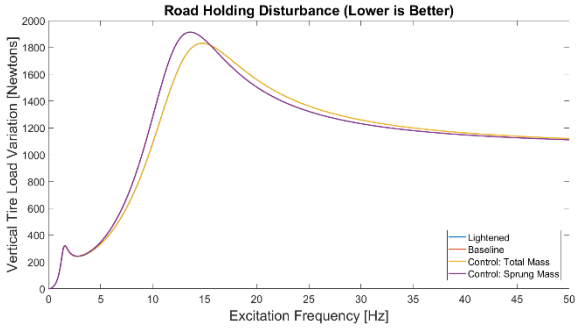

Figure 3. Road holding disturbance of four tested cases across full frequency range

In this graphic (Figure 3), two major relationships can be observed. The total mass control and the lightened unsprung mass case are grouped, while the baseline and the sprung mass control are grouped. Thus, the two cases with a reduced unsprung mass are found to be closely related, while the two cases with the baseline unsprung mass are found to be closely related, implying the most important factor in the simulation was the

unsprung mass. This tends to lend credence to the claim that the observed phenomena are due to the unsprung mass reduction rather than a reduction in overall mass of the system.

At very low excitation frequencies, below 1.7 Hz (Figure 4), the systems behave similarly, however some conclusions can be drawn. In this region, the lightened system exhibits slightly less road holding disturbance than the baseline, thus a handling improvement. The two control cases exhibit a similar behavior yet shifted higher on the vertical tire load variation scale. The total mass control is slightly lower than the sprung mass control. This suggests that while the effect of unsprung mass is a negative influence on the handling in this regime of suspension excitation, the effect of an equal sprung mass increase outweighs the positive effects of the unsprung mass decrease. Thus, unsprung mass reduction is positive under these working conditions, yet not as positive as sprung mass reduction.

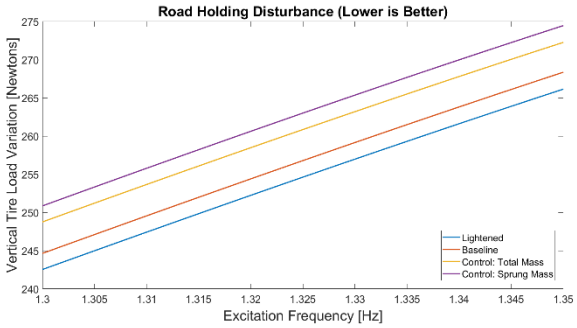

Figure 4. Representative sample of road holding disturbance of four tested cases below 1.7 Hz

At medium frequencies, between 1.7 and 3 Hz (Figure 5), the results are different. While the lightened case is still lower than the baseline, the two controls are shifted lower on the vertical tire load variation scale rather than higher. The total mass control is still lower than the sprung mass control. This reinforces the benefit of the reduction in unsprung mass, yet sprung mass reduction exhibits a negative influence in this region.

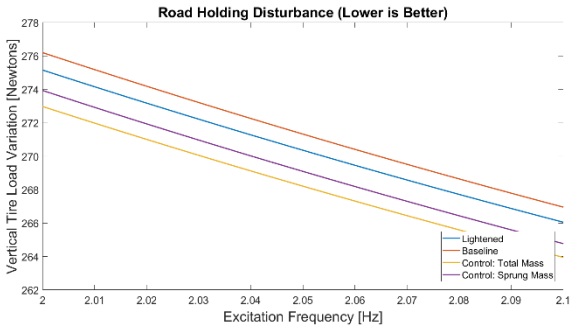

Figure 5. Representative sample of road holding disturbance of four tested cases above 1.7 Hz

At medium frequencies, between 3 and 15.5 Hz (Figure 6), the lightened system exhibits significantly less road holding disturbance than the baseline, up to a 15% decrease. The total mass control case exhibits similar behavior to that of the lightened case, while the sprung mass control case exhibits similar behavior to the baseline case. This highlights that most of the improvement is indeed due to the reduction in unsprung mass. The total mass and sprung mass control cases are, slightly lower than the lightened and baseline cases respectively, demonstrating that sprung mass reduction still has a negative influence in this region. It must be noted that this does not overshadow the effect of reducing unsprung mass, as increasing sprung mass induces a positive effect on the vertical tire load variability in this region, however, has negative effects for overall handling due to inertial effects.

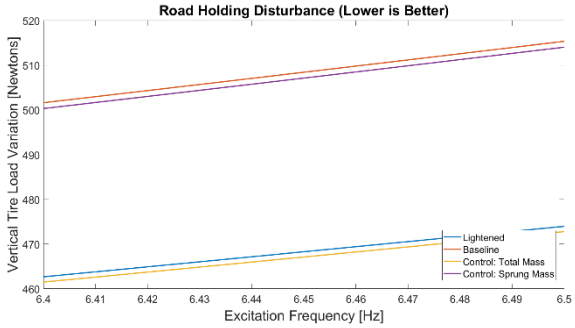

Figure 6. Representative sample of road holding disturbance of four tested cases from 3 to 15.5 Hz

At high frequencies, over 15.5 Hz (Figure 7), the results favor the baseline case. In this region, the lightened system exhibits slightly more vertical tire load variation than the baseline, resulting in worse handling. The total mass control case and the lightened case are practically identical in this region, while the sprung mass control and the baseline case are almost identical as well. This implies the entire effect is due to the change in unsprung mass, and that the sprung mass of the system is irrelevant under these working conditions.

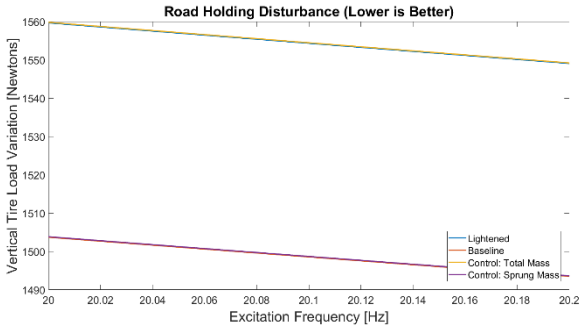

Figure 7. Representative sample of road holding disturbance of four tested cases above 15.5 Hz

The results of the simulation are similar also for occupant discomfort (Figure 8). The results can be broken into four behavior regions as well, with below approximately 1.4 Hz, between 1.4 and 4.5 Hz, between 4.5 Hz and 13.1 Hz, and above 13.1 Hz each exhibiting distinct behaviors.

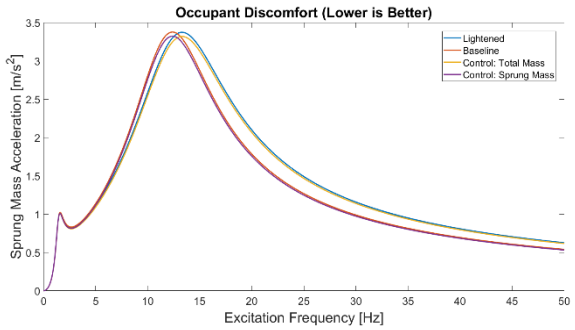

Figure 8. Occupant Discomfort of four tested cases across full frequency range

In this general graphic, two major relationships can be observed. The total mass control and the lightened unsprung mass case are grouped, while the baseline and the sprung mass control are grouped. Thus, the two cases with a reduced unsprung mass are found to be closely related, while the two cases with the baseline unsprung mass are found to be closely related, implying the most important factor in the simulation was the

unsprung mass. This tends to lend credence to the claim that the observed phenomena are due to the unsprung mass reduction rather than a reduction in overall mass of the system.

At very low excitation frequencies, below 1.4 Hz (Figure 9), the systems behave extremely similarly. In this region, the lightened system exhibits slightly less sprung mass acceleration than the baseline, thus a comfort improvement. The two control cases exhibit a similar behavior yet shifted higher on the sprung mass acceleration scale. The total mass control is slightly lower than the sprung mass control. This suggests that while the effect of unsprung mass is a negative influence on comfort in this regime of suspension excitation, the effect of an equal sprung mass increase outweighs the positive effects of the unsprung mass decrease. Thus, unsprung mass reduction is positive under these working conditions, yet not as positive as sprung mass reduction.

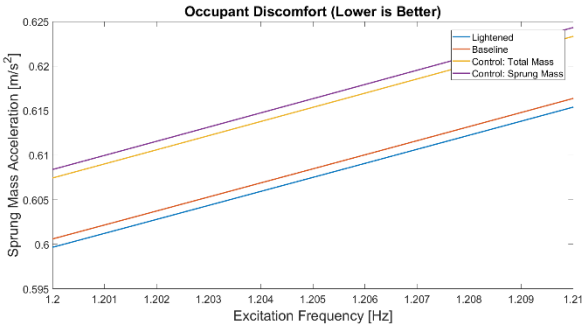

Figure 9. Representative sample of Occupant Discomfort of four tested cases below 1.4 Hz

At medium frequencies, between 1.4 and 4.5 Hz (Figure 10), the results are different. While the lightened case is still lower than the baseline, the two controls are shifted lower on the sprung mass acceleration scale rather than higher. The total mass control is still lower than the sprung mass control. This reinforces the benefit of the reduction in unsprung mass, yet sprung mass reduction switches, and exhibits a negative influence in this region.

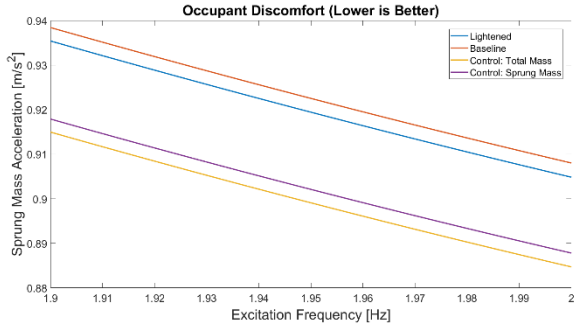

Figure 10. Representative sample of Occupant Discomfort of four tested cases from 1.4 to 4.5 Hz

At medium frequencies, between 4.5 and 13.1 Hz (Figure 11), the lightened system exhibits significantly less occupant discomfort than the baseline, up to an 9% decrease. The total mass control case exhibits similar behavior to that of the lightened case, while the sprung mass control case exhibits similar behavior to the baseline case. This highlights that most of the improvement is indeed due to the reduction in unsprung mass. The total mass and sprung mass control cases are slightly lower than the lightened and baseline cases respectively, demonstrating that sprung mass reduction still has a negative influence in this region. It must be noted that this does not include optimization of damping factors and spring rates, thus the findings on the influence of sprung mass are not as conclusive as those on the unsprung mass (which is more pertinent to this study).

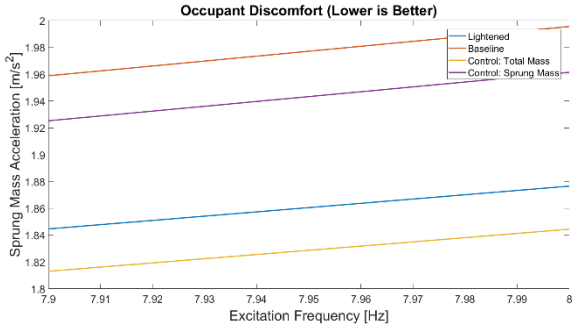

Figure 11. Representative sample of Occupant Discomfort of four tested cases from 4.5 to 13.1 Hz

At high frequencies, over 13.1 Hz (Figure 12), the results favor the baseline case. In this region, the lightened system exhibits slightly more sprung mass acceleration than the baseline, resulting in lower occupant comfort. Thus, at excitation high frequencies, unsprung mass reduction negatively impacts vehicle comfort. Different to the road holding disturbance results, the control cases are slightly lower than their counterparts. This implies that also sprung mass reduction is disadvantageous to comfort at these suspension excitation frequencies yet has less effect than unsprung mass reduction.

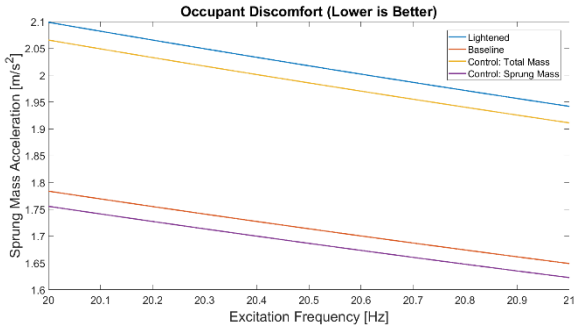

Figure 12. Representative sample of Occupant Discomfort of four tested cases above 13.1 Hz

Considering the observations made above, it is difficult to come to a conclusive decision as to the overall benefit of unsprung mass reduction. For both comfort and handling, certain fascia of excitation frequency favors a heavy unsprung mass, while others benefit from lightening. In general, the lightened unsprung mass was beneficial at lower excitation frequencies, while above 13 to 15 Hz the heavier unsprung mass began to gain an advantage. In the road holding disturbance tests, the lightened unsprung mass holds a large advantage at low frequencies, while the baseline, heavier, unsprung mass hold a small advantage at higher frequencies. Thus, one can already begin to see that, overall, a lighter unsprung mass will be beneficial from this point of view. The comfort tests are less promising, with the lightened unsprung mass holding a small advantage at low frequencies, and the baseline having a large advantage at high frequencies.

This data, however, is of limited scope. The simulations show the behavior of the suspension due to a set of excitation frequencies, yet do not discriminate as to which frequencies are more important. The simulation is a test equally examining all possible working conditions, rather than presenting a true to life working condition based off a typical vehicle usage.

Road Spectrum

To properly determine the real-world benefit of the lightened suspension configuration tested in the previous simulation, the observed behavior is weighted by real world road profile inputs. The road holding disturbance and occupant discomfort levels are determined for each suspension excitation frequency, however the simulation does not account for the varying prominence between these input frequencies.

A road profile's imperfections are a spatial, rather than temporal, feature. A road profile can be described in space by relating wavenumber to wavelength. The equation of the relationship between frequency and wavelength-based road profile according to a selected vehicle speed is presented below in equation 2:

$$\omega = \frac{2\pi}{T} = \frac{2\pi V}{\lambda} = \gamma V \qquad (2)$$

utilizing equation (2), a frequency is obtained from a wavenumber and vehicle speed. The base vehicle speed pertaining to this study is 100 km/h, and ISO standard 8608:1995 "C Road" is used as a standard road profile power spectral density.

The square of the metric (comfort or handling) is multiplied by the spectrum of the surface irregularity to obtain the final weighted average. The result is then normalized, as the actual value is unimportant for the purpose of the study, instead the differences between the different proposed configurations are the only studied factors.

Biological Spectrum

The sprung mass acceleration of the occupant based on the transmissibility of the suspension and the power spectral density of the road profile is a useful metric yet does not focus on the true requirement of the vehicle suspension for human comfort. Comfort is a human sensation, thus quantifying it based on accelerations at various frequencies without quantifying a human sensitivity to these frequencies is of limited use. The value is not in a metric of the acceleration, but in a metric of the human experience in the vehicle.

In this study ISO standard 2631-1:1997/Amd 1:2010 (ISOBio) is used as a basis. This standard outlines the human body's sensitivity to vibrations of various frequencies for comfort, fatigue, and safety. It is a standard particularly aimed at transportation systems. It outlines vibration sensitivities on various parts of the body and with varying direction. In this case, the vibration was taken to be vertical of the whole body in a seated position. The model is working in a purely vertical direction; thus, no other vibrations can be accounted for. The focus on purely vertical motion greatly simplifies the biosensitivity calculations (Figure 13). This is determined to be a reasonable simplification due to the overwhelmingly vertical function of the suspension.

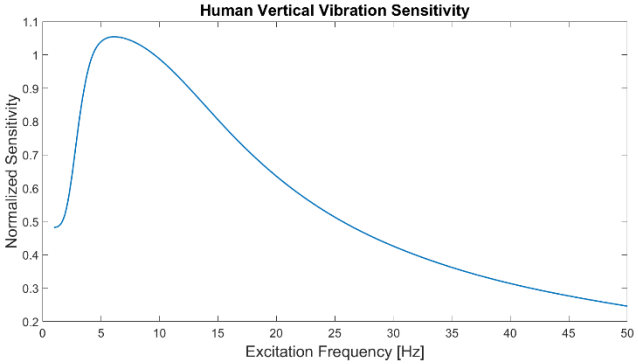

Figure 13. ISO Standard 2631-1:1997/Amd 1:2010 vertical body acceleration comfort sensitivity

It is important to note that this only pertains to the occupant discomfort data acquired earlier from the simulation and then passed through the road spectrum analysis. The human sensitivity to vibration has no bearing on tire distortion, and thus that data is only weighted by the road profile.

Observed Benefits

Vertical tire load variation has improved for both the lightened unsprung mass case and the total mass control. There is a very minor penalty for the sprung mass control. The percentage gain/loss results and the weighted graphs are reported in Table 2 and Figure 14.

Table 2. Road holding disturbance: percent change with respect to Baseline

Lightened	Total Mass	Sprung Mass
-8.81	-8.76	0.4

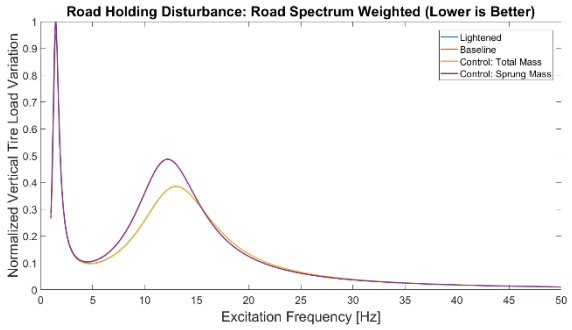

Figure 14. Road Spectrum Weighted Road Holding Disturbance

The minor deterioration between the lightened case and the total mass control, as well as the minor deterioration between the baseline and the sprung mass control shows that most of the improvement is due to the reduced unsprung mass. Unsprung mass has a large negative impact on road holding disturbance, while sprung mass has a relatively small negative impact on road holding disturbance. This shows the handling importance of focusing on unsprung mass reduction, and the benefit of moving to lighter control arms for both performance and safety in real world conditions.

Occupant comfort has improved for all three cases (the lightened unsprung mass, the total mass control, and the sprung mass control). This contrasts with the results of the road holding disturbance tests. The percentage gain/loss results and the weighted graphs are reported in Table 3, and Figure 15.

Table 3. Occupant discomfort: percent change with respect to Baseline

Lightened	Total Mass	Sprung Mass
-5.73	-10.00	-4.63

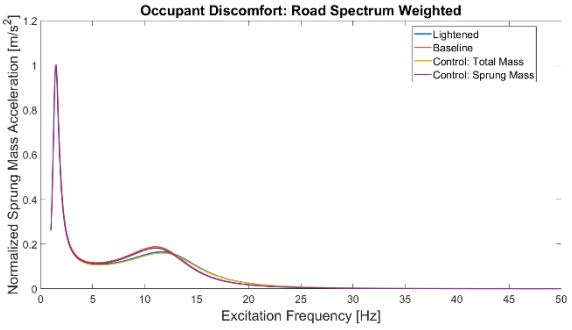

Figure 15. Road Spectrum and Biosensitivity Weighted Occupant Discomfort

The benefits of a reduction in unsprung mass are evident, yet the benefits of an increase in sprung mass are important as well. While the system is much more sensitive to sprung mass for comfort reasons than it is for road holding disturbance reasons, it is still less effective than unsprung mass. Unsprung mass has a large negative impact on occupant comfort, and sprung mass has a positive impact on occupant comfort, of only slightly lower magnitude.

Relative Advantage

It is demonstrated that reducing unsprung mass has a greater benefit than reducing sprung mass even when accounting for typical operating conditions and human sensitivities, yet this is still semi-useful information without weighing its benefit versus a reduction in sprung mass, and considering the differences in benefit/cost ratio between the two.

For road holding disturbance, the results show that the benefit to tire distortion of removing 5 kg of unsprung mass is 220.25 times higher than the benefit of removing 5 kg of sprung mass. While encouraging, it must be noted that the tire distortion caused by road imperfections is only a small component of overall handling. It can be concluded, however, that reducing unsprung mass is a far more effective method of consistently “working” the tires during transient conditions than reducing sprung mass, likely more than the cost difference between the two types of mass reduction.

For comfort, the benefit is non-quantifiable, as while reducing unsprung mass increases comfort, reducing sprung mass is actively detrimental to only a slightly lesser degree. This also could be subject to further study, with the optimization of spring and damper ratios, as well as analyzing the possibility of using less expensive dampers, as they would need to control less mass. Overall, it can be concluded that the reduction of unsprung mass reduces overall mass without compromising ride.

The reduction of unsprung mass is deemed to be of enough benefit to proceed further with the study and move on to more complex simulations and part designs. While expensive, it offers benefits that cannot be found through less expensive forms of mass reduction and could be a useful technology for improving road and race vehicles to meet modern standards.

Multibody Analysis

A virtual model of the car is created in MSC Adams Car software (Figure 16). Basic specifications of the car, such as weight distribution and power are input to the model, as well as suspension details. The suspension hard point locations are determined by processing images of the vehicle subsystem using ImageJ measurement software, as well as using real world measurements. The damping rates, spring stiffness and preload, and antiroll bar stiffnesses are estimated quantities.

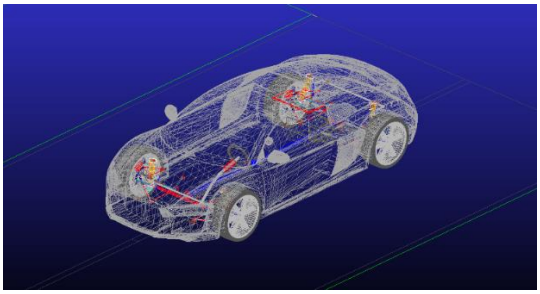

Figure 16. Adams Car Model

These are the same as those used in the quarter car model simulations, however the process is repeated for the rear suspension as well, due to the weight differences between the front and rear of the car, as well as expected natural ride frequencies. The model can be subject to a full array of tests, from maneuvers as simple as open loop step steers, to four post rigs, to closed loop ISO standards. Using the driver software, laps of a complete racetrack can be completed.

Shaker Rig

The shaker rig test available in MSC Adams Car is designed to simulate a classic four post shaker rig. This test emulates the quarter car model that was simulated in Simulink in the pre-engineering phase of this project. The addition of the 4 posts and the full car model allow for more complex interactions. While the car is not moving, there is roll and pitch which are not present in the quarter car model. The full car model with and without the lightened unsprung mass is subject to the 4-post shaker test at the same 0-50 Hz frequencies as the quarter car model, and the same tire distortion (Figure 17) and sprung mass acceleration (Figure 18) values were monitored. For this case, the unsprung mass difference between the baseline case and the lightened case was raised to 20 kg in order to accentuate the effects.

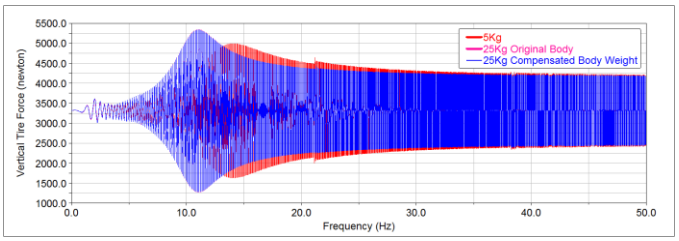

Figure 17. Four Post Shaker Rig Tire Distortion

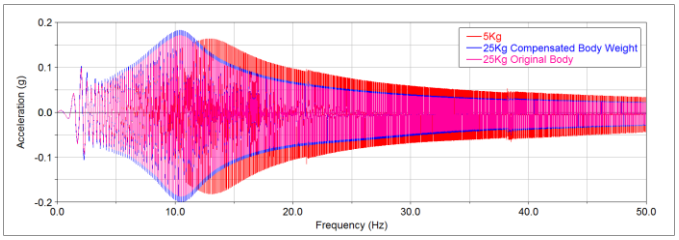

Figure 18. Four Post Shaker Rig Sprung Mass Acceleration

The results are slightly different that those of the quarter car simulation, however the general trends remain. The two main natural frequencies, that of the suspension, and that of the tire, are similar, while the additional ones (those of bushings and other elastic members) are minor. The general trend that the lightened unsprung mass case is of large benefit at low frequencies and begins to become detrimental above 15 Hz is verified. The extent to which the two cases differ is also similar. This validates the quarter car simulation, and the ability to continue with the full car model and continue to more complex situations.

Maneuvers

An ISO 3888-2 double lane change is simulated using the full car model. ISO Standard 3888-2 is a maneuver designed to test obstacle avoidance. It measures sort of transient reaction that may be affected by the reduction of unsprung masses. The transient nature of a double lane change maneuver allows the evaluation of the effect of the unsprung mass reduction effectively.

Two metrics are measured during this simulated maneuver, chassis acceleration along the Y axis, and yaw rate, both for a baseline case and for a case with the unsprung mass reduced by 5 kg (compensated by raising the sprung mass). Chassis acceleration is observed to discern differences in the immediacy of the chassis' development of lateral force. Yaw rate is observed for the to evaluate the immediacy of the chassis' rotation. These are measured to ensure that the yaw rate is producing useful lateral acceleration, rather than a vehicle spin. The choice to observe yaw rate is made as it is a more direct measure of the steering phenomenon of interest, and due to the last measured factor, the phase change of the yaw rate. This is a direct measure of the immediacy of the maneuver.

The lateral acceleration results show a very minor improvement in the responsiveness of the input for the lightened case (Figure 19). This improvement is in the order of 0.005 g, thus too minor to be deemed significant with respect to the errors within the model.

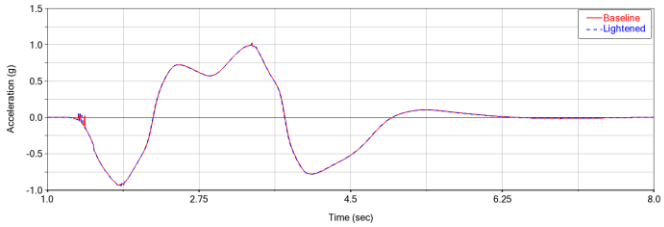

Figure 19. Lateral acceleration during ISO maneuver for baseline and lightened case

Yaw rate results are like one another (Figure 20), except for a slight change in responsiveness. The curves are near identical traces of on another, however the lightened case exhibits a quicker response. In general, the first change of direction occurs 0.01 seconds earlier, and by the second change of direction, the lightened case's advantage has grown to 0.02 seconds.

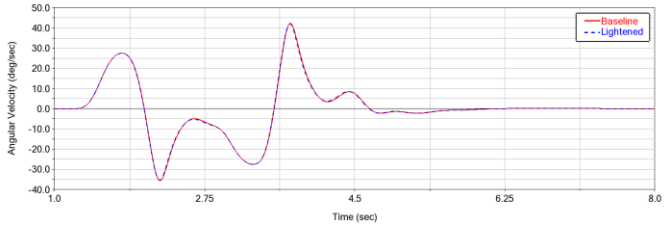

Figure 20. Yaw Rate during ISO maneuver for baseline and lightened case

A second maneuver, a swept-sine steer is simulated to infer under what type of steering inputs the lightened unsprung mass exhibits a benefit. The data from this maneuver can then be used to discern how the vehicle reacts to various frequencies of steering inputs, like the transfer function developed with the quarter car model. This maneuver is simulated at 100 km/h over 20 seconds, with a steering oscillation from 0.5 to 2 Hz at a fixed amplitude of 0.5 g.

A bode plot is created with the results (Figure 21), comparing steering angle to yaw rate. It shows the gain is unchanged at low frequencies but nearing the 2 Hz area the lightened case was shown to have a higher gain by 0.005. This shows that a lightened unsprung mass is more beneficial during faster steering inputs, which supports the previous statements, that unsprung mass will be of importance during transient conditions.

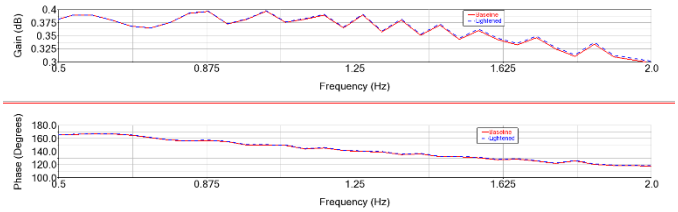

Figure 21. Bode plot of Steering Angle and Yaw Rate during the swept-sine steer maneuver

The results of these simulated maneuvers support previous assumptions of there being a handling and safety benefit to reducing unsprung mass. Unfortunately, this benefit has been seen to be rather small, despite exaggerating the possible reduction in mass. This suggests that while unsprung mass reduction is more beneficial than sprung mass reduction, the difference may not be enough to justify the elevated cost of

reducing unsprung mass compared to that of sprung mass. The study proceeds to developing a normative for the design of a set of composite control arms.

Load Case Development

In order to design the composite front upper control arm, a set of requirements need to be defined and converted into load cases. The expected critical load cases for a suspension arm would be under vehicle braking, cornering, acceleration, and “railroad tie” bump (Figure 22) [18]. The limits can be based on deformations, in the case of location critical hard points, or stresses. In either case, a safety factor is to be applied to ensure there is ample room for part tolerances. To obtain these load cases, a simulation is performed for each maneuver.

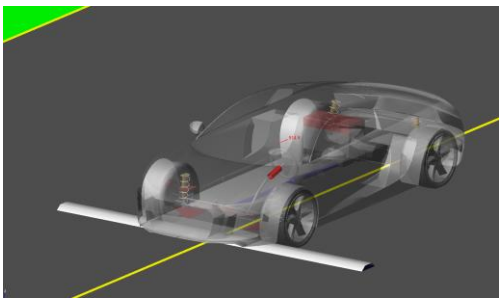

Figure 22. Bump test simulation

In each simulation, the forces at the three attachments of the arm (spherical joint, forward bushing, rearward bushing) are logged, and their maximum recorded. These forces are transformed into load cases by applying the force seen on the spherical joint and fixing the two bushing mounts.

Table 4. Load case forces

Force	Acceleration	Braking	Lateral	Bump	Maintain
F_x	-575	6015	262	-284	-22
F_y	-512	-2313	1213	-1772	-921
F_z	-17	-184	-96	-135	-36

Phase 2: Part Design and Calculation

Construction Methods

A variety of construction methods are considered for the realization of the CFRP control arm [19]. Wet carbon layup, resin infusion, prepreg carbon, and forged/sheet molding compound are each present in industry and could be available for the manufacturing of the arm. Forged/SMC carbon and prepreg carbon were determined to be the two most interesting options, representing two extremes of the cost-spectrum. Seeing as Volkswagen Audi Group has already investigated the use of their forged carbon technology in the construction of control arms, a Solvay Cycom® 2035-42%-T800-2x2T-200 prepreg is selected as the construction material in this study. This product is recommended for automotive and motorsports use, and its properties (Table 5) are readily available [20].

Table 5. Material Properties used in calculations [20]

Property	Room Temperature
E_1 (GPa)	79

E_2 (GPa)	79
Nu_{12}	0.015
G_{12}	4.7
X_t (MPa)	1068
X_c (MPa)	832
Y_t (MPa)	1068
Y_c (MPa)	832
S (MPa)	137
S_B (MPa)	101

The part is constructed without core, apart from in areas where inserts are co-molded. This choice does not optimally utilize the CFRP material, but allows for greatly simplified production, and a similarity with existing, stamped sheet metal parts [21]. This simplification can also result in better part quality.

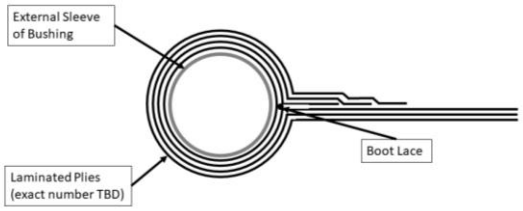

Figure 23. Cross section diagram of laminate in inboard bushing region

The two inboard hardpoints where the arm meets the chassis are equipped with the same type of bushing already present on the in-production aluminum arm. These consist of two concentric steel sleeves with a rubber cylinder in between them. In contrast to the aluminum arm, these are cold bonded to the arm, preventing their replacement, which would be a safety concern. To create the cylindrical feature used to house this bushing, the carbon plies are run long, then folded back over a loose tool in the part mold as shown in figure 23.

The outboard hardpoint uses a conical seat to mount the pin on a typical rubber isolated spherical joint. This is the same part as present in the current vehicle, however the configuration is swapped, with the conical seat on the arm rather than the upright. The conical seat is created using a chopped carbon fiber molded insert, placed midway through lamination as shown in figure 24. This prevents a costly post machining step, and possible exothermic problems when curing a thick ply stack.

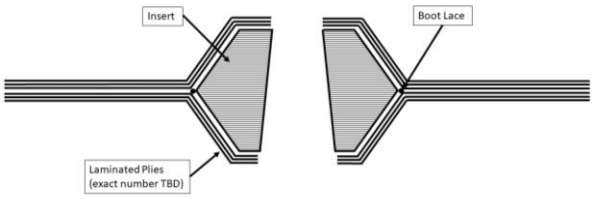

Figure 24. Cross section diagram of laminate in inboard bushing region

Composite Optimization

The calculation and optimization step of this study is run on Altair Optistruct software, and broken into two parts: topology optimization, and topography optimization. The topography optimization can be further broken down into three separate sub-stages: free size, size, and shuffle optimization.

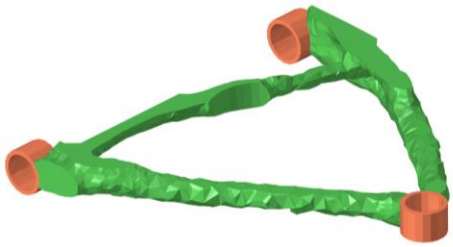

Figure 25. Raw output of the optimization (element density iso-surface of 0.2)

Topology optimization does not immediately lend itself to the creation of a relatively flat structure, as decided upon in the Construction Methods chapter, yet is carried out to visualize the load paths running through the structure [22–24]. A design space and constraint space for the arm is created, and subject to the five load cases developed previously. The design space includes the entire region of the arm plane, apart from where the coil over must pass through to attach to the upright. The constraint space is an area around each of the hardpoints. The resulting element density allows a visualization of which areas of the part are working (Figure 25).

This raw data is run through the OSSmooth feature resulting in a more usable CAD model. This model is imported into Siemens NX software and is used as a guide to create a molded surface of the proposed monolithic “flat” control arm, as well as its inserts (Figure 26).

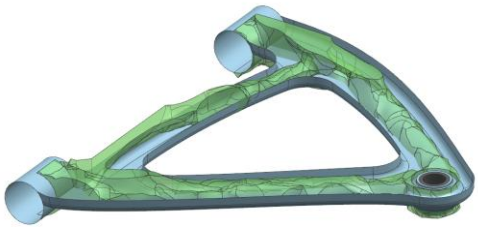

Figure 26. Control arm molded surface with topology optimized overlay

Topography optimization techniques are used to determine the most effective layup for the molded surface developed using the topology optimization. The first of the topography optimizations applied is a Free-Size optimization (Figure 27).

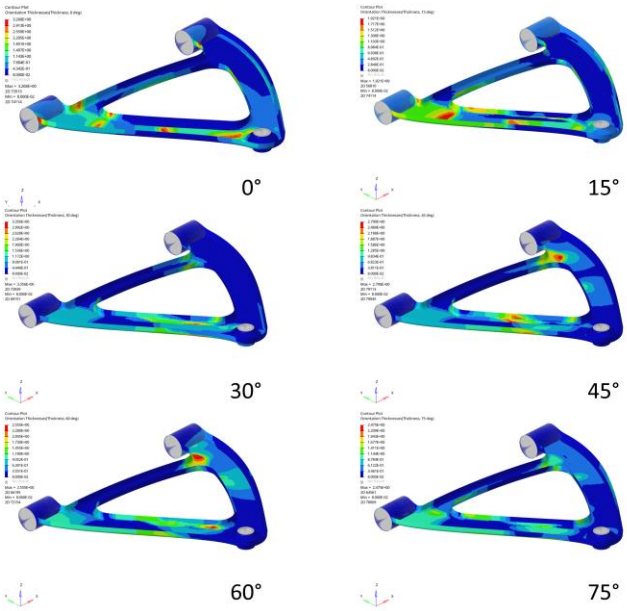

Figure 27. Ply thicknesses for each laminate direction

The next step in the Optistruct composite optimization workflow is a sizing operation (Figure 28).

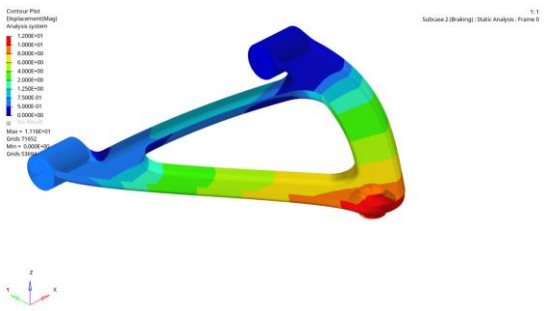

Figure 28. Contour plot of displacement: braking load case (Size optimization)

This is also known as ply shape sizing. This step takes the ply shapes output from the previous optimization step and discretizes them into a manufacturable item. During this step various other manufacturing concerns are accounted for (both automatically and by hand), such as the discrete thickness of each ply, and the achievable ply shapes. In this phase, the 200 g weight constraint is removed, and instead a deformation constraint of 12mm at the outboard hardpoint is enforced. This is chosen as half of that found in Volkswagen Audi Group's own internal studies and should be suitably stiff.

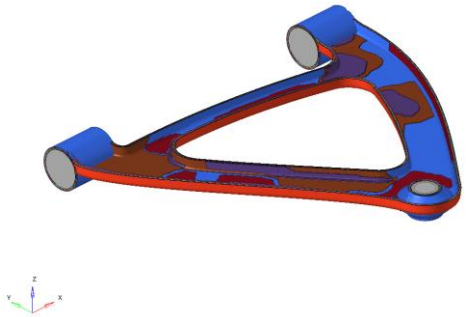

Figure 29. Plies prior to shuffle optimization

Figure 30. Plies after shuffle optimization

The last step of the optimization workflow is a Shuffle, or ply order optimization. This optimization reorders the various plies (Figure 29) and “shuffles” to find an optimal stacking order (Figure 30). Various manufacturing considerations, such as cover plies, and maximum number of successive same-orientation plies can be considered during this phase. In this case, the maximum same orientation plies are set to 4, and two cover plies are specified.

Figure 31. Contour plot of composite ply failure: braking load case (shuffle optimization)

Figure 32. Contour plot of composite bond failure: braking load case (shuffle optimization)

The overall displacement has lowered by 19.8% with respect to the model prior to the stacking optimization. This is evidence that a more efficient ply stacking is achieved. The area of maximum risk to failure (Figure 31 and 32) has reduced, and the minimum strength ratio is raised (Figure 33) compared to previous optimization steps. The minimum strength ratio is under 1, however this area is exceedingly small (isolated elements)

adjacent to constraints and over ply discontinuities and not of concern due to its status because of the calculation model's assumptions.

Figure 33. Contour plot of composite strength ratio: braking load case (shuffle optimization)

Iteration 0	Iteration 59	Legend
1101	2101	75.0 degrees
1102	5402	60.0 degrees
1201	5401	45.0 degrees
2101	5405	30.0 degrees
2102	1101	15.0 degrees
3101	1102	0.0 degrees
3102	6102	
4101	2102	
5101	6101	
5102	5303	
5201	5201	
5301	5302	
5302	5301	
5303	1201	
5401	5102	
5402	5101	
5403	5403	
5404	5404	
5405	3102	
6101	4101	
6102	3101	

Figure 34. Ply stack sequence before and after optimization

These small areas of minor concern have, however, both reduced in size and magnitude during the optimization, suggesting an overall improvement in the efficiency of the usage of material post-shuffle optimization (Figure 34). The buckling load factor has increased to 3.8, again suggesting a more effective usage of material.

Phase 3: Production Preparation

Production Tooling

A geometry model of the production mold is created. Steel will be used, as it is the most durable, and best choice for serial production molds. The mold consists of thirteen parts (Figure 35): a base, four loose tools with one fixing each, and a locating bolt and nut. The four loose tools allow the formation of the cylindrical bushing retention area. The locating bolt and nut allow the secure location of the insert for the spherical joint. The left and right mold could be integrated to one another; however, this would increase the mold weight past the standard 30kg for a normal worker to lift by hand and therefore make transferring to the autoclave a more involved process.

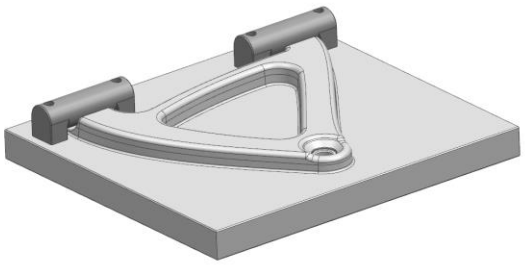

Figure 35. Main mold and loose tools

Production Steps

After the molds are produced, the creation of the part starts with material preparation. A worker cuts the carbon plies from a roll of carbon fabric kept in a freezer. This roll must be equalized to temperature over the course of 3 to 4 hours in a sealed bag to avoid condensation and water contamination (creates voids during the curing process). This fabric is then be draped over a plotter and the individual shapes will be cut. Depending on the shapes, up to 75% usage is not out of the ordinary. After this step is completed, the individually cut plies are organized, bagged, and delivered to a clean room for lamination. Simultaneously, the mold and loose tools are prepared, with release wax being sprayed or brushed onto the entirety of the molding face. This wax ensures the part is not ruined during the post-cure extraction process. Also, the co-molded insert is to be pressed and delivered to the lamination room.

When both the prepared mold and plies are available, the lamination begins. In this case, due to the serial production nature of this part, a ply positioning system is a reasonable fixed cost to assume, as it aids the laminator in placing the plies, negating the need for templates, both speeding the lamination time and reducing errors. Plies one through ten are laminated directly on to the mold. These must be laminated far enough past the edge of the part that they reach the horizontal surface of the mold return. Next, the insert is placed into its receptacle and secured with the locking bolt and nut, through to the bottom of the mold. Now the rest of plies (through to ply twenty-one) are laminated over the previous ones, trapping the insert in the middle. During the previous lamination steps, care is taken to leave long, undamaged, “tails” of unused material on all the plies where they meet the cylindrical bushing area of the control arm. The loose tools are placed and secured with each of their M6 shoulder bolts, locating them precisely with respect to the main tooling. The “tails”, which were left long previously, are then folded back over the top of the loose tool and re-laminated to the main body of the arm in a staggered fashion.

The exposed carbon part is covered in release film to keep the bagging material from adhering to it during the cure. Breather material is placed over the release film to aid in air evacuation. Lastly, the part is vacuum bagged, placing the vacuum hose attachment over the flat surface of the mold runout. The part is delivered to the autoclave area, where it is hooked to the vacuum for an hour to ensure the bagging has no leaks, then placed in the machine for a cure cycle. The standard cure cycle for this material is to raise the temperature 2°C per minute to 135°, apply 689 kPa of pressure, hold at 135° for 120 minutes, then cool to below 60° at 3° per minute.

After the part is cool enough to work with, it is taken to a trimming area for extraction. This extraction consists of undoing the five fixing bolts and removing the part. If removing the fixing bolts does not cause the part to “pop” off the mold, the area of the horizontal return which has been laminated serves to allow a sacrificial “pry” area and remove the part forcefully. After it is removed, a rotary cutting tool is used to trim the area laminated on the mold returns to a scribe line integrated into the molding face denoting the intended part edge. The two rubber/metallic cylindrical bushings are now cold bonded into their cylindrical seats (which, like the flange area, have been given a draft to aid in their installation). Lastly, it is delivered to the production line for assembly on the car.

Conclusion

A complete workflow for the engineering of a composite upper control arm for a performance vehicle is demonstrated. At this level of development, the study represents an extended feasibility study. This workflow follows the broad steps which would be used in industry, starting with justification, moving on to design, and finishing with production analysis.

The development of the part is justified in that it represents a notable benefit compared to the lightening of similar, but unsprung parts. The benefit of reducing unsprung mass on tire distortion attributed to average road imperfections is found to be 220 times higher than that of reducing sprung mass. The benefit of reducing unsprung mass on occupant comfort is found to be even higher, because reducing sprung mass (the only other option compatible with vehicle light weighting philosophies) is actively detrimental. The cost-benefit ratio of this design approach is called into question due to the high cost of weight reduction in the unsprung areas, however this decision be left to the client – who nonetheless benefits from having options.

The design of the part is carried out with composite optimization technologies to fully exploit the characteristics of carbon fiber reinforced polymer. The optimized part successfully reduces mass of the final part by an estimated 41.2%. Furthermore, the deflection at the hard points is 63% less than that exhibited by the aluminum part. The part is successfully designed to take advantage of the orthotropic properties of the material, rather than use the carbon fiber reinforced polymer as simple semi-isotropic “black metal”.

From the outset, the part is imagined keeping production in mind, as this is often more critical than the part itself in composite design. Mold geometry is created, and production steps are defined.

More importantly than each individual phase, tools, procedures, and know-how are successfully developed to ease the repetition of this exercise for different vehicles and clients. Possible future improvements to the process could be: an elaboration of the Simulink model to include further degrees of vehicle freedom and various excitement modes, implementation of full composite strength ratio response and manufacturing constraints for non-standard ply orientations in the composite optimization to lessen user involvement (available in more recent software releases), and the development of a cost analysis study in partnership with potential manufactures.

References

1. Ferraris, A., Messana, A., Multari, D., Sisca, L., Airale, A.G., and Carello, M., “Steering System of a Low-Consumption Vehicle: From the Dynamics Analysis to the Design of the Wheel Assembly,” in: Carbone, G. and Gasparetto, A., eds., *Advances in Italian Mechanism Science*, Springer International Publishing, Cham, ISBN 978-3-030-03319-4: 91–99, 2019, doi:10.1007/978-3-030-03320-0_10.
2. Ferraris, A., Micca, F., Messana, A., Airale, A.G., and Carello, M., “Feasibility Study of an Innovative Urban Electric-Hybrid Microcar,” *Int. J. Automot. Technol.* 20(2):237–246, 2019, doi:10.1007/s12239-019-0023-x.
3. Messana, A., Sisca, L., Ferraris, A., Airale, A.G., Carvalho Pinheiro, H. de, Sanfilippo, P., and Carello, M., “From Design to Manufacture of a Carbon Fiber Monocoque for a Three-Wheeler Vehicle Prototype,” *Materials* 12(3):332, 2019, doi:10.3390/ma12030332.
4. Carello, M., Airale, A.G., and Messana, A., “IDRApegasus: a carbon fiber monocoque vehicle prototype,” *Mater. Werkst.* 45(5), 2014, doi:10.1002/mawe.201400238.
5. Carvalho Pinheiro, H. de, Messana, A., Sisca, L., Ferraris, A., Airale, A.G., and Carello, M., “Computational Analysis of Body Stiffness Influence on the Dynamics of Light Commercial Vehicles,” in: Uhl, T., ed., *Advances in Mechanism and Machine Science*, Springer International Publishing, ISBN 978-3-030-20131-9: 3117–3126, 2019, doi:10.1007/978-3-030-20131-9_307.
6. Carello, M., Ferraris, A., Airale, A.G., Messana, A., Sisca, L., Pinheiro, H. de C., and Reitano, S., “Experimental Characterization of Piezoelectric Transducers for Automotive Composite Structural Health Monitoring,” *SAE Int. J. Adv. Curr. Pract. Mobil.* 2(5):2553–2567, 2020, doi:10.4271/2020-01-0609.

7. Carello, M. and Airale, A.G., “Composite Suspension Arm Optimization for the City Vehicle XAM 2.0,” in: Öchsner, A. and Altenbach, H., eds., *Design and Computation of Modern Engineering Materials*, Springer International Publishing, Cham, ISBN 978-3-319-07382-8: 257–272, 2014, doi:10.1007/978-3-319-07383-5_18.
8. Xu, S., Ferraris, A., Airale, A.G., and Carello, M., “Elasto-kinematics design of an innovative composite material suspension system,” *Mech. Sci.* 8(1):11–22, 2017, doi:10.5194/ms-8-11-2017.
9. Chirwa, E.C., “Crashworthiness of Vehicle Composite Panels and Components,” *Proc 5th Jpn. Int. SAMPE Symp.* 1194, 1997.
10. Carello, M., Airale, A.G., Ferraris, A., Messana, A., and Sisca, L., “Static Design and Finite Element Analysis of Innovative CFRP Transverse Leaf Spring,” *Appl. Compos. Mater.* 24(6), 2017, doi:10.1007/s10443-017-9596-6.
11. Messana, A., Ferraris, A., Airale, A.G., Fasana, A., and Carello, M., “Enhancing Vibration Reduction on Lightweight Lower Control Arm,” *Shock Vib.* 2020:1–15, 2020, doi:10.1155/2020/8891831.
12. Anderson, M. and Harty, D., “Unsprung Mass with In-Wheel Motors - Myths and Realities,” *Protean Serv. - Available Httpswwwproteanelectriccomf201804protean-Serv.*, 2018.
13. Ferraris, A., Pinheiro, H.D.C., Galanzino, E., Airale, A.G., and Carello, M., “All-Wheel Drive Electric Vehicle Performance Optimization: From Modelling to Subjective Evaluation on a Static Simulator,” *2019 Electric Vehicles International Conference, EV 2019*, undefined-undefined, 2019, doi:10.1109/EV.2019.8893027.
14. Carvalho Pinheiro, H. de, Ferraris, A., Galanzino, E., Sisca, L., Carello, M., Airale, A., and Messana, A., “All-wheel drive electric vehicle modeling and performance optimization,” *SAE Tech. Pap. Ser.*, 2019, doi:https://doi.org/10.4271/2019-36-0197.
15. Carvalho Pinheiro, H. de, Messana, A., Sisca, L., Ferraris, A., Airale, A.G., and Carello, M., “Torque Vectoring in Electric Vehicles with In-wheel Motors,” in: Uhl, T., ed., *Advances in Mechanism and Machine Science*, Springer International Publishing, ISBN 978-3-030-20131-9: 3127–3136, 2019, doi:10.1007/978-3-030-20131-9_308.
16. Milliken, W.F., “Race Car Vehicle Dynamics,” Society of Automotive Engineers, ISBN 978-0-7680-0103-7, 1995.
17. Butkunas, A.A., “Power Spectral Density and Ride Evaluation,” SAE Technical Paper 660138, 1966, doi:10.4271/660138.
18. Papacz, W., Kuryło, P., and Tertel, E., “The Composite Control Arm – Analysis of the Applicability in Conventional Suspension,” *Am. J. Mech. Eng.* 1(7):161–164, 2013, doi:10.12691/ajme-1-7-1.
19. Friedrich, K. and Almajid, A.A., “Manufacturing Aspects of Advanced Polymer Composites for Automotive Applications,” *Appl. Compos. Mater.* 20(2):107–128, 2013, doi:10.1007/s10443-012-9258-7.
20. CYCOM 2035 data sheet, https://www.solvay.com/en/product/cycom-2035, Oct. 2020.
21. Feraboli, P., Gasco, F., Wade, B., Maier, S., Masini, A., and DeOto, L., “Lamborghini ‘forged composite®’ technology for the suspension arms of the Sesto Elemento,” *ASC conference proceedings*, 2011.
22. Yoo, S., Doh, J., Lim, J., Kang, O., Lee, J., and Kang, K., “Topologically optimized shape of CFRP front lower control ARM,” *Int. J. Automot. Technol.* 18(4):625–630, 2017, doi:10.1007/s12239-017-0062-0.
23. Heo, S.J., Kang, D.O., Lee, J.H., Kim, I.H., and Darwish, S.M.H., “Shape optimization of lower control arm considering multi-disciplinary constraint condition by using progress meta-model method,” *Int. J. Automot. Technol.* 14(3):499–505, 2013, doi:10.1007/s12239-013-0054-7.
24. Fuchs, H. and Salmon, R., “Lightweight MacPherson Strut Suspension Front Lower Control Arm Design Development,” 2011-01–0562, 2011, doi:10.4271/2011-01-0562.

Contact Information

Massimiliana Carello
massimiliana.carello@polito.it

Henrique de Carvalho Pinheiro
henrique.decarvalho@polito.it

Alexander Freedman
alexfreed@gmail.com

Alessandro Ferraris
alessandro.ferraris@polito.it

Andrea Giancarlo Airale
andrea.airale@polito.it